

**A photometric stereo-based 3D imaging system using computer vision and deep learning
for tracking plant growth**

Gytis Bernotas^{1*}, Livia C T Scorza^{2*}, Mark F Hansen^{1*}, Ian J Hales¹, Karen J Halliday²,
Lyndon N Smith¹, Melvyn L Smith¹, Alistair J McCormick^{2,†}

¹ Centre for Machine Vision, Bristol Robotics Laboratory, University of the West of England,
T block, Frenchay Campus, Coldharbour Lane, Bristol, BS16 1QY, UK

² SynthSys & Institute of Molecular Plant Sciences, School of Biological Sciences, University
of Edinburgh, Edinburgh, EH9 3BF, UK

*co-first authors ; † Corresponding author

Article type: Research

Email addresses

Authors:	Emails	ORCID
Gytis Bernotas:	gytis.bernotas@uwe.ac.uk	0000-0002-3418-5758
Livia C T Scorza:	livia.scorza@ed.ac.uk	0000-0002-0145-3592
Mark F Hansen:	mark.hansen@uwe.ac.uk	0000-0003-4681-6251
Ian J Hales:	ian.hales@brl.ac.uk	0000-0001-5828-4745
Karen Halliday:	karen.halliday@ed.ac.uk	0000-0003-0467-104X
Lyndon N Smith:	lyndon.smith@uwe.ac.uk	
Melvyn L Smith:	melvyn.smith@uwe.ac.uk	
Alistair McCormick:	alistair.mccormick@ed.ac.uk	0000-0002-7255-872X

†corresponding author:

Dr Alistair J. McCormick

Daniel Rutherford Building, SynthSys & Institute of Molecular Plant Sciences

School of Biological Sciences, University of Edinburgh

The King's Buildings, EH9 3BF Phone: +44 (0)1316505316

Abstract

Background: Tracking and predicting the growth performance of plants in different environments is critical for predicting the impact of global climate change. Automated approaches for image capture and analysis have allowed for substantial increases in the throughput of quantitative growth trait measurements compared to manual assessments. Recent work has focused on adopting computer vision and machine learning approaches to improve the accuracy of automated plant phenotyping. Here we present PS-Plant, a low-cost and portable 3D plant phenotyping platform based on an imaging technique novel to plant phenotyping called photometric stereo (PS).

Results: We calibrated PS-Plant to track the model plant *Arabidopsis thaliana* throughout the day-night (diel) cycle and investigated growth architecture under a variety of conditions to illustrate the dramatic effect of the environment on plant phenotype. We developed bespoke computer vision algorithms and assessed available deep neural network architectures to automate the segmentation of rosettes and individual leaves, and extract basic and more advanced traits from PS-derived data, including the tracking of 3D plant growth and diel leaf hyponastic movement. Furthermore, we have produced the first PS training data set, which includes 221 manually annotated *Arabidopsis* rosettes that were used for training and data analysis (1768 images in total). A full protocol is provided, including all software components and an additional test data set.

Conclusions: PS-Plant is a powerful new phenotyping tool for plant research that provides robust data at high temporal and spatial resolutions. The system is well-suited for small and large-scale research and will help to accelerate bridging of the phenotype-to-genotype gap.

Keywords

Arabidopsis thaliana, leaf angle, segmentation, machine learning, near-infrared (NIR) LEDs, photomorphogenesis, thermomorphogenesis.

Introduction

Quantitative and accurate methods are required to aid strategies for predicting plant growth performances in our changeable natural environments. Such tools are critical for calibrating predictive models in the face of a changing global climate and our growing global population [1–6]. Computer vision is an evolving technology that is helping to drive advances in plant phenotyping both in fundamental research and agriculture [7–10]. Reflecting its considerable promise, effort has been directed toward automated ground vehicles (AGVs) [11,12], satellite [13], drone [14] and gantry-style platform imaging of field plants [15], and automated phenotyping of greenhouse [16,17] and lab-grown plants (the challenges are different for field and indoor phenotyping) [18,19]. While there have been significant advances, problems associated with high cost, automated data capture, large data sets and variable visual and temporal resolutions have created barriers to the uptake of these technologies. These challenges are currently being addressed in the next generation of plant phenotyping tools.

Above ground growth is a strong indicator of plant yield and therefore 3D imaging of vegetative growth is a very active area of phenotyping research [20–25]. A number of excellent 2D imaging systems have been developed [26–28], however, while they represent a qualitative improvement on manual data capture, they have limited capacity to resolve plant architecture at high resolution. For example, leaf area measurements are affected by blade curvature, leaf angle and movement, making accurate estimations of plant growth challenging using 2D [9,29]. Several 3D imaging methods have been developed that overcome some of the limitations of

2D. These can be classified as passive and active 3D imaging approaches and are briefly outlined below.

Passive 3D imaging approaches capture plant architecture without introducing new energy (e.g. light) into the environment [30]. Methods and technologies using this approach include multi-view stereo [31,32], of which the most common is binocular stereo [33,34], structure from motion [35], light-field (plenoptic) cameras [36], and space carving approaches [37]. Passive approaches that use two or more sensors, or have moving parts (e.g. robot arm or gantry systems), often encounter difficulties in identifying and aligning the same points in different images (i.e. the so called ‘correspondence problem’), which can result in imprecise reconstruction of 3D shapes [38]. Plant leaves and canopies can be particularly challenging as they often represent large homogenous areas with little salient texture. Imprecise 3D reconstructions can be smoothed, but at the expense of plant surface detail [39]. Space carving overcomes the correspondence problem, but requires many different views of an object and may still fail to reconstruct crowded areas (e.g. overlapping leaves) [37]. To our knowledge, only light-field cameras have been utilised successfully for capturing 3D plant growth throughout the diel (day-night) cycle [36,40]. However, light-field systems rely on expensive camera technology to capture high-resolution data, and like other passive approaches, require consistent and favourable lighting conditions.

Active 3D imaging approaches emit energy (e.g. light), which can overcome several problems associated with passive approaches. Structured light [41] and laser scanners [42–44] are active technologies that rely on triangulation to determine the point locations in a 3D space. Both methods can provide high-quality 3D reconstructions of plant canopy architecture, but structured light approaches require very accurate correspondence between images while laser

scanners can be slow, and can potentially heat or even damage plants at high frequencies [45]. Furthermore, triangulation techniques are susceptible to occlusions (e.g. other objects in the environment or leaf overlap) that can reduce data quality. Time of Flight (ToF) cameras (e.g. LiDAR) comprise another active 3D imaging approach that determine the distance of a point directly from the time delay between an emitted light pulse and its reflection. However, the resolution of ToF cameras is still relatively low, which has tended to limit its use to imaging larger plants [46,47]. Although both passive and active 3D imaging approaches can significantly improve the accuracy of plant growth measurements and even expand on the architectural traits available to capture compared to 2D imaging, existing 3D imaging techniques still lack in several crucial areas such as speed, availability, portability, spatial resolution and cost [25].

Photometric Stereo (PS) is an active imaging technique that is low-cost and can achieve high image resolutions and fast capture speeds [48]. This approach has been applied only recently to plant phenotyping and has shown significant promise [49]. PS relies on a set of images of an object captured under controlled, varied and directional illumination (Fig. 1; Supplementary Information S1). The obtained images are then used to generate a dense surface normal (SN) map of matching resolution, where each pixel represents a normal vector's components (i.e. the orientation in three cardinal directions - x, y and z) that allows the overall orientation of the object to be determined. Prior work has shown that plant leaf SN data acquired by PS can be captured at high resolutions (4.1 megapixel (MP)), and thus has significant advantages in encoding complex 3D morphology to aid challenging automated recognition and quantification tasks, such as the extraction of plant growth data [49,50].

Machine learning is now emerging as a promising field to transform the automation of trait extractions from plant image data sets [51,52]. Work in the model plant *Arabidopsis thaliana*

(hereafter Arabidopsis) has revealed much about the molecular processes underlying the relationship between leaf area, biomass and yield [53], and several methods have been developed for automating data extraction from Arabidopsis images [54–56]. Recently, significant advances have been made in the development of artificial neural networks (NNs) for automated segmentation of the rosette and individual leaves, and leaf counting using 2D image data [57–59]. However, the performance of NN approaches for leaf segmentation, for example, are still limited by a need for large annotated data sets for training, as models trained with small-scale databases typically generalise weakly. To our knowledge, currently there are no NN models optimised for leaf segmentation using 3D data. A subsequent challenge is accurate object tracking to enable segmented leaves to be tracked across different time points of a data set [60,61].

Here we present a novel, low-cost imaging system called PS-Plant that for the first time utilises PS for monitoring the growth and development of Arabidopsis in 3D. We compared the accuracy of 3D vs 2D data from PS-Plant for estimating leaf area, angle, and rosette growth against ground truth measurements and showed comparable results to the state-of-the-art 3D light-field camera and laser scanning systems [36,43,44]. To demonstrate the versatility of PS-Plant, we analysed growth under a matrix of different conditions that illustrate the dramatic effect of the environment on the 3D phenotype of a wild-type Arabidopsis plant. Furthermore, we showed that 3D data from PS-Plant can be used to train NN models for automated leaf segmentation of a growing rosette, as an important first step in extracting plant features. Finally, we demonstrated that utilisation of machine learning for leaf segmentation and PS data can be combined to extract useful growth traits related to dynamic leaf movement and rosette development.

Results and discussion

Photometric stereo imaging using PS-Plant provides accurate spatial data for Arabidopsis plants

PS-Plant consists of a machine vision camera surrounded by four or eight Near Infrared (NIR) Light Emitting Diodes (LEDs) and a bespoke LED controller that allows rapid switching of the LEDs for high temporal data acquisition (Fig. 1A-C; Supplementary Data S1). PS-Plant can acquire up to 40 2D images per second at a spatial resolution of 2048×2048 pixels. The acquisition process takes 125-225 milliseconds per set of PS images, followed by *ca.* 5 s to process the 2D images to compute SN map estimations and 3D surface integration (Supplementary Information S1 and S2). A NIR filter positioned in front of the lens provides consistent contrast and brightness for images captured throughout the diel cycle. The camera provides a 17 x 17 cm field of view that allows simultaneous tracking of up to nine Arabidopsis plants in 5 x 5 cm pots. Growth data sets for individual plants were extracted from each master image experiment data set using a Python-based GUI software. Overall, PS-Plant is portable and light-weight (*ca.* 7 kg without a PC) and could be adjusted to fit in different growth environments including growth cabinets or greenhouse environments. At the time of manufacture, the total cost for PS-Plant was approximately US\$3,200.

A key assumption in PS is that the surface of the imaged object should exhibit Lambertian reflectance (i.e. it reflects light equally in all directions, while the reflected intensity diminishes according to the Lambert's cosine law) (Supplementary Information S1) [48]. As the reflectance of the object deviates from the Lambertian model, the subsequent estimation error increases accordingly. To verify if PS-Plant could accurately estimate total area and angle of an object, we initially used rectangular flat pieces of acrylic of known area (600 mm^2) covered in white matte paper, which achieved a close approximation of Lambertian reflectance [62],

and imaged with a black matte background to facilitate image segmentation [63]. The acrylic objects were placed on laser cut wedges to allow imaging at a range of known angles (Fig. 2A). The projected areas were estimated using 2D and 3D data obtained from PS-Plant. The 3D data enabled us to estimate the object inclination angles, which were compared to the ground truth (Fig. 2B). Using 3D data, the area was estimated accurately up to 45° with a Mean Relative Error (MRE) of 1.0% (see Supplementary Information S3 for formulas). In contrast, estimates based on 2D data became inaccurate at inclinations greater than 10° , with a MRE of 10.3% when all angles were considered. Angle estimations consistently matched the known angle for all inclinations tested with a Mean Absolute Error (MAE) of 0.89° . These results highlighted the accuracy of PS-Plant in estimating the angle and area of a flat object in 3D space.

Next, we investigated Arabidopsis rosettes in PS-Plant and observed that Arabidopsis leaves exhibited near Lambertian reflectance under NIR light (Supplementary Information S1). We hypothesised that longer wavelengths penetrate deeper into the leaf and are then typically scattered, rather than specularly reflected at the leaf surface [64,65]. Similarly to the object area and angle estimation experiment, we imaged Arabidopsis rosettes inclined from 0° to 45° using a rotary inclination table and compared the estimated areas using 2D and 3D data with ground truth measurements of the imaged rosettes (Fig. 2C). Even without inclination (i.e. at 0°) estimates based on 3D data were more accurate compared to those from 2D data, indicating that the former was more capable of approximating areas for complex objects that include a degree of surface topographic relief (e.g. an Arabidopsis rosette). 3D data continued to outperform 2D data at increased inclinations with a MRE of 4.5% and 18.1% for 3D and 2D estimations, respectively. The accuracy of 3D estimations did decrease at angles $>30^\circ$ due to the increase in leaf (self-) occlusion that occurred when the whole rosette was inclined (Supplementary Information S4). When the accuracy of angle estimations was tested with

selected individual leaves from the Arabidopsis rosettes (Fig. 2D), PS-Plant achieved a MAE of 3.8° for leaf angle estimations. We observed that the estimated and known leaf inclination angle correlated in the mid-range (10 to 30°) but less so at lower and higher angles. This was likely due to the natural curvature of Arabidopsis leaves compared to a flat surface, as Arabidopsis leaf blades typically have a convex shape when observed from above. Therefore, when the leaves were not inclined (i.e. at 0°), the estimated angles were still higher than zero as they were calculated from the varying SN values across each leaf blade surface.

PS-Plant enables accurate 3D reconstructions of growing Arabidopsis rosettes

Following validation, we assessed the accuracy and consistency of PS-Plant in monitoring plant growth and mean rosette inclination over time (Fig. 3). PS-Plant captured both 2D and 3D data for Arabidopsis plants for 12 days, starting from 11 days after germination (DAG) in standard growth conditions (22 °C, 150 $\mu\text{mol photons m}^{-2} \text{s}^{-1}$, 12 : 12 hr light : dark). The automated image capture program resulted in a SN map produced for each plant every 30 minutes that was used to characterise rosette surface curvature (Fig. 3A) as described in Supplementary Information S1. Furthermore, SN data could be used to derive rosette surface inclination angles and concavity/convexity values. Such information can be used, for example, in leaf developmental analysis to evaluate perturbances in normal leaf abaxial / adaxial expansion [66,67].

Both 2D and 3D data sets produced exponential growth curves for projected rosette area (PRA) that were typical for Arabidopsis growth (Fig. 3B). However, 2D data consistently underestimated PRA and showed erroneous reductions in area estimates consistent with rhythmic nastic leaf movements (Fig. 3C, D; Supplementary Data S2). In contrast, 3D data accounted for leaf curvature and movement (Supplementary Information S1), such that PRA

increased more smoothly over the time course of the experiment. The small decreases observed for PRA from 3D data were associated with self-occlusion at high leaf inclination angles (as in Fig. 2). A number of studies have shown that growing *Arabidopsis* leaves exhibit rhythmic movement that is controlled by the circadian oscillator [68–71]. PS-Plant estimations of rosette surface inclination (i.e. the total inclination of all rosette leaf blades and petioles) is able to accurately record this rhythmicity, which in our 12L:12D conditions achieved an amplitude peak at 4-6 hr post dusk (Fig. 3D) (calculated using BioDare2; see Materials and Methods). Interestingly, our data showed that leaf rhythmicity appears to be anticipatory up to 16 DAG, after which it was strictly diurnal. As older plants have a higher proportion of mature leaves, that are no longer elongating, our data suggests that these leaves still exhibit rhythmic movements but they are driven by the daily light-dark cycle rather than the circadian oscillator. These data highlight the capability of PS-Plant to not only provide accurate area estimates, but to capture leaf movement rhythms that are regulated by the circadian clock and the prevailing photoperiod.

Rosette architectural parameters derived from 2D data were also obtained from PS-Plant, including circularity (or stockiness), compactness, diameter and perimeter (Fig. 3E-H) [36,72,73]. These data showed, for example, an increase in perimeter and diameter that was consistent with plant growth, and a decrease in compactness, which was associated with elongation of leaf petioles as the rosette developed.

PS-Plant reveals 3D growth traits for Arabidopsis plant grown in different environments

We next wanted to establish whether PS-Plant could capture alterations in growth plasticity induced by changes in the external light and temperature environment. Low levels of photosynthetic active radiation are known to elicit a shade avoidance response (SAR), where

plants exhibit elongated stems and petioles, increased hyponasty and smaller and fewer leaves [74–76]. As high temperatures to some extent target the same molecular pathways, heat also elicits an SAR-type response [77,78]. These studies illustrate that the growth strategy adopted by the plant is strongly dependent on the surrounding light environment and the ambient temperature. To capture these morphological changes we tracked Arabidopsis plants under nine conditions that differed in temperature [17 (LT), 22 (LT) and 27°C (HT)] and light intensity [40 (LL), 150 (ML) and 300 $\mu\text{mol photons m}^{-2} \text{s}^{-1}$ (HL)] (Fig. 4A; Supplementary Fig. S1; Data S3).

Plants grown in LL had small leaves, recorded as low PRA, which was comparable in plants grown at different temperatures. Increases in light levels led to a concomitant rise in PRA, however, over light intensities of 150 $\mu\text{mol m}^{-2} \text{s}^{-1}$ the PRA was strictly temperature-dependent with the highest PRA achieved at the highest light and temperature (Fig. 4B). The observed differences in PRA were reasonably consistent with overall biomass accumulation at 24 DAG (Fig. 4C, D). Notably, in ML plants a shift from 17°C to 22°C led to an increase in biomass, while a shift from 22°C to 27°C did not. Although we have not measured leaf thickness, previous work has shown that plants grown in high temperatures tend to have thinner leaves and a higher specific leaf area (the ratio of leaf area to dry mass) [79,80], which could explain the increase in area from 22°C to 27°C but no increase in biomass. HL and ML plants produce more leaves at 22°C compared to 17°C, signifying a larger investment in vegetative growth. Plants grown at 27°C induced flowering in HL and ML plants and so their final leaf number was slightly lower than at 22°C (Fig. 4E).

Together, these results could be explained by the thermodynamic relationship between the dark reactions (e.g. Rubisco activity and the Calvin cycle) and light reactions of photosynthesis. The

assimilation rate of CO₂ by Rubisco is temperature-dependent, such that increased temperatures (up to *ca.* 30 °C) typically correlate with increased CO₂ assimilation in C3 plants grown under non-limiting light conditions [81–83]. These photochemical processes most likely underlie the light- and temperature-dependent changes in PRA and investment in leaf biomass production. Contrasting with this, in LL the supply of ATP and NADPH to the Calvin cycle by the light reactions may have constrained CO₂ uptake, and thus growth rates were not increased by higher temperatures.

PS-Plant also captured differences in petiole length. Analysis of the ML and HL illustrated that increased temperature stimulated petiole elongation in these plants. This is evident in PS-Plant measurements of plant compactness. However, this data also show that HL plants are generally more compact than ML (Supplementary Fig. S2), and that temperature-mediated differences in compactness are less evident in plants grown in HL. This indicates that plants tend to invest more in leaf expansion compared to petiole elongation under higher light intensities.

We then compared the relative expansion rate (RER) based on 3D PRA data for different light-temp conditions over the diel cycle (Fig. 4F-H). RER data for *Arabidopsis* vary between different studies, but generally have comparable rates within light and dark periods for wild-type plants grown under standard growth conditions [9,36,43,84]. In the present study, RER in the dark period was not significantly different across all growth conditions tested [as determined by one-way ANOVA ($p < 0.05$), followed by Tukey's HSD tests]. This was not unexpected, as the rate of leaf starch turnover during the night is known to be maintained over a wide range of environmental conditions and temperatures in *Arabidopsis* [85,86]. RER values during the light period were comparable for plants grown in ML and plants grown in HL-MT and HL-LT. In contrast, HL-HT plants showed an increase RER in the light compared to the

dark period. As HL-HT plants also had the highest biomass accumulation (Fig. 4D), results obtained with PS-Plant suggest HL-HT plants were limited more by carbon turnover than CO₂ assimilation. All plants grown in LL had a significantly decreased RER in the light compared to the dark period. Notably, temperature had no impact on RER in the light for LL plants, indicating that photosynthetic growth was primarily limited by the low irradiance. Further studies on carbon allocation and starch turnover should be carried to complement these observations and hypotheses generated using PS-Plant data.

The internal circadian clock in plants has a periodicity close to 24 hr that can be entrained by environmental cues [87]. Thus, we next used PS-Plant to examine the rhythmicity of total leaf movement (i.e. rosette surface inclination, see Fig. 3D) to compare the capacity of entrainment of the clock to different growth conditions (Fig. 5A-C; Supplementary Fig. S3) [68]. We compared three standard parameters: period, phase and amplitude [87,88].

As expected, all conditions showed a similar period for leaf movement of *ca.* 24 hr ($p < 0.05$) as all plants were grown in a 12 : 12 hr light : dark cycle (Fig. 5D). However, phase and amplitude differed between growth conditions. Through all conditions peak phase occurred during the night, with the general observation that incremental rises in light intensity led to a phase delay in the peak. A possible exception is that in 17°C HL rhythms peaked at the end of the day. It is noteworthy that the 17°C ML and HL leaf rhythm traces are very low amplitude, most likely because these plants had very limited petiole growth. We also found that temperature effects the phase of the rhythm across all light conditions. For example, in both ML and HL growth at 27°C advanced the peak phase compared to 22°C.

Monitoring plant behaviour through time revealed the impact on light and temperature through development (Supplementary Fig. S3). A common trend is that warm temperatures increase mean rosette leaf inclination angle, or hyponasty, though the threshold for this response varies in the different light treatments. Another notable feature is that hyponasty and rhythm amplitude dampen over time. Our data show that under LL the leaf movement rhythms are more sinusoidal and higher amplitude rhythms than in ML and HL. Leaf movement rhythm waveforms of ML and HL are also quite different from LL, with some evidence of tracking dawn and dusk. Interestingly in HL the rhythm at 17°C is clearly in antiphase with 22°C and 27°C. Through time the 17°C rhythm dampens to high leaf hyponasty, while 22°C/ 27°C leaf rhythms dampen to a low leaf angle. In both cases this effect appears to arise from a gradual reduction in rhythmic regulation during the night period. Overall, these data illustrate that PS-Plant is able to extract quantitative data on a large range of traits associated with rhythmic leaf growth that are typically challenging to capture.

Use of PS-Plant data and machine learning for accurate leaf segmentations

Our next goal was to examine the capacity of PS-Plant to track the phenotypic behaviour of individual leaves on a growing Arabidopsis rosette. To achieve this, we labelled individual leaves in 221 images of ML-MT rosettes (Supplementary Information S5) and used machine learning approaches to segment leaves. We compared two available NN architectures, the end-to-end recurrent neural network with recurrent attention (RNN) [58] and the Mask R-convolutional neural network (R-CNN) [89], to examine the suitability of PS-Plant data for NNs designed for instance segmentation using RGB images. We focused on ML-MT plants as their growth was more uniform across different individuals compared to other growth conditions, which allowed the models to converge faster and achieve better results during the training process. The data set was split into 179 and 42 images (approx. 80: 20 ratio) for training

and validating the models, respectively. To avoid overfitting the model, we manually partitioned plant images for training and validation data sets to ensure that all time-series images of a single specimen appear in either training or validation data sets, but not both.

PS-Plant produces a range of different data: from grayscale images to SN maps (e.g. Fig. 3). We trained the RNN and R-CNN architectures from initial random weights, while R-CNN was also pre-trained using transfer learning weights generated using the COCO data set [90]. The RNN and R-CNN architectures were trained using three different types of PS data to compare for segmentation accuracy: i) composite (SN in x and y direction, and albedo for RGB layers), ii) grayscale, and iii) albedo images. All data used for training, including the raw PS-Plant data and rosette masks are available as outlined Supplementary Information S5. The obtained leaf segmentations were compared to the ground truth images using Symmetric Best Dice (SBD; score of the accuracy of leaf instance segmentation) and Foreground-Background Dice (FBD; score of the accuracy of rosette segmentation) evaluation formulas (Supplementary Information S3) [91].

The type of PS data used did not significantly influence SBD or FBD scores, suggesting that accuracy of RGB-based models was not affected by the different types of PS-based data. The most accurate leaf segmentation results were achieved with models based on the R-CNN architecture using pre-trained weights (Fig. 6; Table 1), resulting in SBD scores that ranged from 0.806 (composite image) to 0.814 (albedo). In comparison, the RNN architecture resulted in lower SBD scores of 0.440 (composite image) and 0.560 (albedo and grayscale). The pre-trained R-CNN model also achieved the most accurate rosette segmentation results, with FBD scores ranging from 0.94 (albedo) to 0.946 (grayscale). In contrast, FBD scores for the RNN model varied from 0.798 (composite image) to 0.891 (albedo), indicating that the relative

performance of the RNN architecture was worse for both leaf and rosette segmentation with our data sets when compared to the R-CNN approach.

Table 1. Performance comparison of leaf instance segmentation for two different machine learning architectures. The Mask R-CNN [89] and RNN [58] architectures were trained with composite (SN in x and y direction, and albedo for RGB layers), grayscale or albedo images. The training procedure for the RNN architecture was the same as proposed by the authors [58], while the Mask R-CNN was as follows: head layers for 10 epochs at 10^{-2} Learning Rate (LR); all layers for 30 epochs at 10^{-2} LR, 30 epochs at 10^{-3} LR, 30 epochs at 10^{-4} LR, and head layers for 10 epochs at 10^{-4} LR. The Mask R-CNN was trained both from initial random weights and from pre-trained model weights, while RNN was only trained from initial random weights. Abbreviations: SBD, Symmetric Best Dice; FBD Foreground-Background Dice.

Image type	Mask R-CNN				RNN	
	<u>Random weights</u>		<u>Pre-trained weights</u>		<u>Random weights</u>	
	<u>SBD</u>	<u>FBD</u>	<u>SBD</u>	<u>FBD</u>	<u>SBD</u>	<u>FBD</u>
Grayscale	0.813	0.942	0.812	0.946	0.556	0.866
Albedo	0.758	0.913	0.814	0.940	0.560	0.891
Surface normal map	0.789	0.922	0.806	0.941	0.440	0.798

Using PS-Plant data for dynamic tracking of individual leaf growth and movement

We next investigated the performances of four different approaches for tracking leaves using the segmented image data sets (e.g. Fig. 6): i) kernelized correlation filters [92], ii) optical flow [93], iii) multiple instance learning tracker [94], and iv) a particle filter [95]. Object tracking, especially with partially or even completely occluded objects, is one of the most challenging

areas in computer vision [60,61]. Tracking Arabidopsis leaves over time is particularly challenging due to changes in both shape and movement during growth together with associated occlusions (Supplementary Information S4). The best results were achieved with a particle filter based on leaf instance centroid location and velocity across the time-series images (Fig. 7). Leaf overlap remained a limitation, as an occluding leaf was sometimes assigned the label of an occluded leaf. However, erroneous labelling was found to be infrequent and straightforward to manually corrected *post hoc*, resulting in a robust semi-automated leaf tracker (Supplementary Data S4).

Once we were confident that we could reliably track individual leaves using PS-Plant, we separated leaf blades and petioles by applying a morphological opening function with a predefined radius (3 to 11 pixels based on the leaf size) to the leaf binary mask. The point of differentiation (P_B) is the mean x and y coordinates of the leaf blade and petiole (Fig. 8A). This enabled separate examinations of leaf blade and petiole traits. We then derived separated tissue-specific data including leaf blade area and inclination angle, and leaf blade and petiole length. The angle of leaf blade inclination was estimated using two different methods: i) a point-based approach where leaf blade angle was determined using SN data across the line from P_B to the leaf tip (P_T), and ii) the mean surface inclination of the whole leaf blade. Both methods produced similar results (Supplementary Fig. S4). However, we chose to use the latter (ii) as the P_B was not always visible due to leaf occlusions or the petiole being too small to be distinguished (e.g. maturing leaves or leaves grown in low temperature).

To demonstrate our approach, we tracked leaves 1 to 4 of plants grown in ML at three different temperatures from 15 to 18 DAG. Leaves 1 to 4 were chosen as representative examples of maturing (1 and 2) and immature (3 and 4) leaves (Fig. 8; Supplementary Data S5A-D).

Consistent with our findings for PRA under different growth conditions (Fig. 4; Supplementary Fig. S1), the leaf blade areas of maturing and immature leaves from HT plants were significantly larger than leaf blades from MT and LT plants [as determined by one-way ANOVA ($p < 0.05$), followed by Tukey's HSD tests; Fig. 8B]. The latter results confirmed that the increased PRA observed using PS-Plant for plants grown in HT plants was specifically associated with an increase in leaf blade area. Leaves that emerged prior to the start of the experiment at 11 DAG (i.e. leaf 1) showed an increase in leaf blade area in HT plants compared to MT and LT plants (Fig. 8B). However, leaves that emerged after 11 DAG (i.e. leaf 4) had an even more dramatic growth response to increased temperatures. For example, the blade area for leaf 1 and 4 at 17 DAG was 40% and 130% higher in HT compared to LT, respectively. Similarly, the mean surface inclination of leaf blades was higher in HT (Fig. 8C). The latter result was also consistent with our findings for whole rosette surface inclination at higher temperatures (Fig. 3; 5; Supplementary Fig. S3).

We then calculated parameters associated with diurnal movement for individual leaf blades (Fig. 8D). We targeted immature leaf blades as their movement patterns were clearer and more consistent compared to maturing leaf blades. Period or phase measurements from immature leaf blades were generally similar between growth conditions and comparable to values for whole rosettes (Fig. 5). In contrast, measurements of immature leaf blade amplitude were significantly enhanced at MT and HT and generally higher than values for whole rosettes. This was not unexpected as immature leaves are more active than older leaves and contribute more to overall whole rosette amplitude (see Supplementary Data S3 and S5). Furthermore, the observed temperature-associated increases in amplitude and leaf hyponasty were consistent with whole rosette data (Fig. 5D; Supplementary Fig. S3B). Thus, we concluded that measurements of periodic rhythms can be performed reliably with PS-Plant data using whole

rosettes or individual leaf blades. The values obtained in the present study for period and phase are comparable to those reported for wild-type plants under standard growth conditions by other automated top-down systems for monitoring leaf movement, such as OSCILLATOR [96].

Finally, we used PS-Plant to reveal whether petiole elongation showed a similar response to temperature as the leaf blade by comparing the ratio of leaf blade and petiole length from maturing and immature leaves (Fig. 8E). Petioles have been shown to elongate faster at higher temperatures [77,80,97]. In the present study we observed that leaves from MT and LT plants had a blade: petiole length ratio that ranged from 2: 1 to 4: 1. Immature leaves did not have a detectable petiole under LL, thus only maturing leaves were included at LT. In contrast, HT plants had ratios of approximately 1: 1 for both maturing and immature leaves, indicating that HT resulted in an increase petiole elongation relative to leaf blade growth under ML. Future work should examine this ratio at different light intensities, as petioles and leaf blades are known to have different responses to light. For example, petioles are known to elongate faster under low light while leaf blades grow more slowly [78,98].

Conclusion

In this paper, we have introduced an adaptable and low-maintenance platform for affordable, advanced image-based phenotyping. A key goal was to ensure accessibility to the research community. In this regard, PS-Plant can be considered a powerful, alternative solution to 3D systems based on laser scanning and light-field camera technologies [36,43], which is particularly well suited for setup in low-income or developing countries. Our system exploits the richer data provided by PS-Plant with a combination of traditional image processing and machine learning techniques to extract rosette and leaf-level measurements in an automated

manner. Here, we have demonstrated that PS-Plant is able to accurately monitor several growth traits and diurnal rhythms of different phenotypes of Arabidopsis plants produced in response to varied environments. This provides credibility that future work with PS-Plant will produce robust data for a wide variety of mutant phenotypes. Additionally, the concomitant quantification of overall growth, leaf traits and circadian rhythms can facilitate a better understanding of the relationships among environment, plant yield and internal molecular networks. Previous work has also highlighted that PS can capture high-resolution 3D surface details of leaf surface structures, such as leaf curvature and trichomes, which could be used to investigate dynamic changes in leaf development [50]. Research in plant phenotyping needs to focus on increasing accessibility and instituting effective data standards and management practices to assist with improving plant productivity and genetic gain [99,100]. To help accelerate the latter, we have provided the PS training imaging data set from this study for community access (Supplementary Information S5) and a detailed protocol for software usage and data analysis with a test experimental data set (Supplementary Information S6). In its current design, PS-Plant is optimal for measuring growth traits in rosette-shaped plants such as Arabidopsis. However, we believe it can also be used during the seedling stage of other eudicot species (e.g. tomato, cabbage, oilseed rape) to analyse circadian rhythms by observing the rhythmic movements of cotyledons. Future work with PS-Plant will focus on improvements in leaf tracking [101], integration with spectral information [102], and incorporation of a low-cost depth camera to combine the high resolution of PS with a lower resolution depth map to characterise whole plants with more complex architectures.

Materials and Methods

Plant materials

Arabidopsis (*Arabidopsis thaliana* (L.) Heynh. Col-0) wild-type seeds were stratified for 2-3 days at 4 °C. Each seed was placed in a square pot (50 mm) containing F2+S compost (Levington) covered in acrylic black felt fabric with a central hole (5 mm) and germinated at 22 °C under white light ($150 \mu\text{mol photons m}^{-2} \text{s}^{-1}$ at the plant level) in 12 : 12 hr light : dark for 10 d in a Percival growth cabinet (SE-41AR2). For the plant area validation experiment, the plants were kept in this cabinet for 22 DAG. For imaging with PS-Plant, the seedlings were transferred to a Snijders growth cabinet (Microclima MC1000).

PS-Plant hardware

PS-Plant consists of a machine vision NIR monochrome camera (Grasshopper3 GS3-U3-41C6NIR-C, FLIR Systems Inc., Canada) with a 16 mm fixed focal length lens (Kowa 1"SC LM25SC, Kowa Company Limited, Japan) with a NIR filter attached (LP920, MidOpt, Illinois, USA), four or eight NIR LEDs (PowerStar IR 940 nm, Intelligent LED Solutions, UK), and an in-house designed LED controller that allows rapid switching of LEDs using an Arduino platform (MKRZero, Arduino, Italy). The camera and LEDs were fixed on a square acrylic sheet (44×44 cm) and positioned at a height of 40 cm above the imaging plants (Fig. 1B, C). The camera was positioned centrally in the sheet and the LEDs were positioned around the camera at 45° angle increments. The LEDs were tilted at a 30° angle to illuminate the area under the camera field of view (Fig. 1B). The base of the rig was painted matt black to limit the introduction of specularities from the background. A PC laptop (K501UQ-DM050T, AsusTek Computer Inc., Taiwan) was used to control LED illuminations, and acquire, store and process images using GUI software written in Python. Details on rig assembly and the LED controller design are outlined in Supplementary Information S2.

Leaf movement rhythm analysis

The leaf movement rhythm analysis was performed using the mean inclination angles (whole rosette or individual leaf blade) as an input for BioDare2 beta (<https://biodare2.ed.ac.uk/>). The data was treated with baseline detrending prior to period, phase and amplitude estimations, which was done using the MFourFit algorithm [88].

AVAILABILITY OF SUPPORTING DATA

The training data set supporting the results of this article is available in an Edinburgh DataShare repository (<https://datashare.is.ed.ac.uk/handle/10283/3280>) and outlined in Supplementary Information S5. This data set represents approximately 0.4% of the 50,625 images captured during the “matrix” growth experiment (see Fig. 4A). A user protocol is available in Supplementary Information S6 to assist with software installation (all software is available at <https://bit.ly/2EFOk0O>, the PS-Plant software RRID number is SCR_017032) and provides detailed instructions from image capture through to dynamic growth analyses. Furthermore, a test data set is available in the Edinburgh DataShare repository (<https://datashare.is.ed.ac.uk/handle/10283/3279>).

ADDITIONAL FILES

Supplementary Information S1. Overview of 2D image data processing captured using PS-Plant.

Supplementary Information S2. Overview of the PS-Plant hardware.

Supplementary Information S3. Formulas.

Supplementary Information S4. Area estimation errors.

Supplementary Information S5. PS-Plant training data set description.

Supplementary Information S6. PS-Plant protocol.

Supplementary Figure S1. Rosette and individual leaf growth analysis.

Supplementary Figure S2. Rosette compactness for plants grown in different conditions.

Supplementary Figure S3. Mean rosette surface inclinations for all growth conditions separated by light treatment.

Supplementary Figure S4. Estimated leaf inclination of leaf 1 in medium light and 27°C.

Supplementary Data S1. Interactive 3D model of the PS-Plant system. The model is provided as an .stl file (Rich Media 1.stl), an online link to zoomable, colour version can be found here: <https://bit.ly/2GXNhLy>.

Supplementary Data S2. Comparison of Arabidopsis growth from 2D and 3D data. The graph (top) includes standard deviation of PRA data for three plants growing under conditions outlined in Fig. 3. Examples of plant growth are shown below for 2D [albedo; bottom left (see Supp. Info. 1 for details)] and surface normal map data (bottom right).

Supplementary Data S3. Arabidopsis plants grow and move differently under different light and temperature conditions. Examples of (A) surface normal models or (B) greyscale images for plants of the same age under each growth conditions tested (see Fig. 4) are shown from 11 to 24 DAG.

Supplementary Data S4. Automated tracking of individual Arabidopsis leaves. Example of leaf label tracking following rosette segmentation of a ML-MT plant shown from 15 to 18 DAG. Note that leaves retained the same colour after tracking (right).

Supplementary Data S5. Using PS-Plant for automated tracking of individual Arabidopsis leaf movement in 3D. Four videos illustrate leaf blade tracking of leaves 1 to 4, respectively, for a plant grown in ML-MT from 15 to 18 DAG. Each video shows a trail of leaf blade centroid movement (red dots) on an albedo 2D video (top left). Blue dots illustrate leaf blade movement on 2D x-y (bottom left) and y-z projections (bottom right), and a 3D x-y-z graph (top right).

DECLARATIONS

List of abbreviations

2D: two dimensional; 3D: three dimensional; ANOVA: analysis of variance; AGV: automated ground vehicles; COCO: common objects in context database; DAG: days after germination; FBD: foreground-background dice score; GUI: graphical user interface; HL: high light; HSD: Tukey's honest significant difference test; HT: high temperature; LED: light emitting diode; LiDAR: distance measurement method using pulsed laser light; LL: low light; LR: Learning Rate; LT: low temperature; MAE: mean absolute error; ML: medium light; MP: megapixel; MRE: mean relative error; MT: medium light; NIR: near-infrared; NN: neural network; P_B: leaf base point, or intersection point between leaf blade and petiole; PC: personal computer; P_O: rosette origin point; PRA: projected rosette area; PS: photometric stereo; P_T: leaf tip point; R-CNN: short for Mask R-CNN NN architecture; RER: relative expansion rate; RGB: red, green and blue channels, or a colour image; RNN: short for end-to-end instance segmentation with recurrent attention NN architecture; SAR: shade avoidance response; SBD: symmetric best dice score; SD: standard deviation; SN: surface normal; ToF: time of flight.

Consent for publication

This study abides by UK guidelines and legislation for plant science research.

Competing interests

The authors declare that they have no competing interests.

Funding

This work was supported by the UK Biotechnology and Biological Sciences Research Council grants BB/N02334X/1, BB/M025551/1 and BB/N005147/1. GB was funded by the University of the West of England (UWE) Partnership Fund.

Authors' contributions

GB, MFH and IJH designed the hardware and software of PS-Plant system including the image processing pipeline. AM, KJH and LCTS designed the plant experimental setup. GB and LCTS performed and analysed the validation experiments. LCTS performed and analysed plant growth experiments. GB designed the study for NN model generation for leaf segmentation. AM, LCTS and GB wrote the manuscript, with assistance from all authors. AM, LNS and MLS supervised the project.

Acknowledgements

We thank Jackie Aim and Stewart Cromar (University of Edinburgh) for assistance with the process of 3D model designs.

REFERENCES

1. Meinke H. Agricultural impacts: Europe's diminishing bread basket. Nat Clim Chang. 2014;4:541–2.
2. Long SP, Marshall-Colon A, Zhu XG. Meeting the global food demand of the future by engineering crop photosynthesis and yield potential. Cell. 2015;161:56–66.
3. Chew YH, Wenden B, Flis A, Mengin V, Taylor J, Davey CL, et al. Multiscale digital Arabidopsis predicts individual organ and whole-organism growth. Proc Natl Acad Sci. 2015;112:E2556.
4. Elliott J, Deryng D, Müller C, Frieler K, Konzmann M, Gerten D, et al. Constraints and

618 potentials of future irrigation water availability on agricultural production under climate
619 change. *Proc Natl Acad Sci.* 2014;111:3239–44.

620 5. Cang FA, Wilson AA, Wiens JJ. Climate change is projected to outpace rates of niche
621 change in grasses. *Biol Lett.* 2016;12:20160368.

622 6. Liang X-Z, Wu Y, Chambers RG, Schmoldt DL, Gao W, Liu C, et al. Determining climate
623 effects on US total agricultural productivity. *Proc Natl Acad Sci.* 2017;114:2285–92.

624 7. Ahmad J, Sun J, Smith L, Smith M. Improving photometric stereo through per-pixel light
625 vector calculation. *Br Mach Vis Conf.* 2013;1–12.

626 8. Furbank RT, Tester M. Phenomics - technologies to relieve the phenotyping bottleneck.
627 *Trends Plant Sci.* 2011;16:635–44.

628 9. Dobrescu A, Scorza LCT, Tsaftaris SA, McCormick AJ. A “Do-It-Yourself” phenotyping
629 system: Measuring growth and morphology throughout the diel cycle in rosette shaped plants.
630 *Plant Methods.* 2017;13:1–12.

631 10. Shakoor N, Lee S, Mockler TC. High throughput phenotyping to accelerate crop breeding
632 and monitoring of diseases in the field. *Curr Opin Plant Biol.* 2017;38:184–92.

633 11. Underwood J, Wendel A, Schofield B, McMurray L, Kimber R. Efficient in-field plant
634 phenomics for row-crops with an autonomous ground vehicle. *J F Robot.* 2017;34:1061–83.

635 12. Ruckelshausen A, Biber P, Dorna M, Gremmes H, Klose R, Linz A, et al. BoniRob: an
636 autonomous field robot platform for individual plant phenotyping. *Precis Agric.* 2009;9:841–
637 7.

638 13. Tattaris M, Reynolds MP, Chapman SC. A Direct Comparison of Remote Sensing
639 Approaches for High-Throughput Phenotyping in Plant Breeding. *Front Plant Sci.* 2016;7:1–
640 9.

641 14. Sankaran S, Khot LR, Espinoza CZ, Jarolmasjed S, Sathuvalli VR, Vandemark GJ, et al.
642 Low-altitude, high-resolution aerial imaging systems for row and field crop phenotyping: A

643 review. *Eur J Agron.* 2015;70:112–23.

644 15. Virlet N, Sabermanesh K, Sadeghi-Tehran P, Hawkesford MJ. Field Scanalyzer: An
 645 automated robotic field phenotyping platform for detailed crop monitoring. *Funct Plant Biol.*
 646 2017;44:143–53.

647 16. da Costa RMF, Simister R, Roberts LA, Timms-Taravella E, Cambler AB, Corke FMK,
 648 et al. Nutrient and drought stress: implications for phenology and biomass quality in
 649 miscanthus. *Ann Bot.* 2018;XX:1–14.

650 17. Tester M, Awlia M, Brown T, Wilson P, Rungrat T, Trtilek M, et al. Using Phenomic
 651 Analysis of Photosynthetic Function for Abiotic Stress Response Gene Discovery. *Arab B.*
 652 2016;14:1–12.

653 18. Tardieu F, Cabrera-Bosquet L, Pridmore T, Bennett M. Plant Phenomics, From Sensors
 654 to Knowledge. *Curr Biol.* 2017;27:770–83.

655 19. Araus JL, Kefauver SC. Breeding to adapt agriculture to climate change: affordable
 656 phenotyping solutions. *Curr Opin Plant Biol.* 2018;1–11.

657 20. Sharma RC. Selection for biomass yield in wheat. *Euphytica.* 1993;70:35–42.

658 21. Richards RA. Selectable traits to increase crop photosynthesis and yield of grain crops. *J*
 659 *Exp Bot.* 2000;51:447–58.

660 22. Arora VK, Singh CB, Sidhu AS, Thind SS. Irrigation, tillage and mulching effects on
 661 soybean yield and water productivity in relation to soil texture. *Agric Water Manag.*
 662 2011;98:563–8.

663 23. Zhang H, Flottmann S. Seed yield of canola (*Brassica napus* L .) is determined primarily
 664 by biomass in a high- yielding environment. *Crop Pasture Sci.* 2016;67:369–80.

665 24. Zhang H, Flottmann S. Genotypic variation in the accumulation of water-soluble
 666 carbohydrate in canola and its potential contribution to seed yield in different environments.
 667 *F Crop Res.* 2016;196:124–33.

668 25. Vázquez-Arellano M, Griepentrog HW, Reiser D, Paraforos DS. 3-D imaging systems for
669 agricultural applications—a review. *Sensors (Switzerland)*. 2016;16.

670 26. Green JM, Appel H, Rehrig EM, Harnsomburana J, Chang JF, Balint-Kurti P, et al.
671 PhenoPhyte: A flexible affordable method to quantify 2D phenotypes from imagery. *Plant*
672 *Methods*. 2012;8:1–12.

673 27. Dhondt S, Gonzalez N, Blomme J, De Milde L, Van Daele T, Van Akoleyen D, et al.
674 High-resolution time-resolved imaging of in vitro *Arabidopsis* rosette growth. *Plant J*.
675 2014;80:172–84.

676 28. Minervini M, Giuffrida M V., Perata P, Tsiftaris SA. Phenotiki: an open software and
677 hardware platform for affordable and easy image-based phenotyping of rosette-shaped plants.
678 *Plant J*. 2017;90:204–16.

679 29. Chen JM, Black TA. Defining leaf area index for non-flat leaves. *Plant Cell Environ*.
680 1992;15:421–9.

681 30. Bianco G, Gallo A, Bruno F, Muzzupappa M. A comparative analysis between active and
682 passive techniques for underwater 3D reconstruction of close-range objects. *Sensors*
683 *(Switzerland)*. 2013;13:11007–31.

684 31. Pound MP, French AP, Fozard JA, Murchie EH, Pridmore TP. A patch-based approach to
685 3D plant shoot phenotyping. *Mach Vis Appl*. 2016;27:767–79.

686 32. Pound MP, French AP, Murchie EH, Pridmore TP. Automated Recovery of Three-
687 Dimensional Models of Plant Shoots from Multiple Color Images. *Plant Physiol*.
688 2014;166:1688–98.

689 33. Biskup B, Scharr H, Schurr U, Rascher U. A stereo imaging system for measuring
690 structural parameters of plant canopies. *Plant, Cell Environ*. 2007;30:1299–308.

691 34. Burgess AJ, Retkute R, Pound MP, Mayes S, Murchie EH. Image-based 3D canopy
692 reconstruction to determine potential productivity in complex multi-species crop systems.

693 Ann Bot. 2017;119:517–32.

694 35. Jay S, Rabatel G, Hadoux X, Moura D, Gorretta N. In-field crop row phenotyping from
695 3D modeling performed using Structure from Motion. Comput Electron Agric. 2015;110:70–
696 7.

697 36. Apelt F, Breuer D, Nikoloski Z, Stitt M, Kragler F. Phytotyping^{4D}: A light-field imaging
698 system for non-invasive and accurate monitoring of spatio-temporal plant growth. Plant J.
699 2015;82:693–706.

700 37. Gibbs J, Pound M, French A, Wells D, Murchie E, Pridmore T. Plant Phenotyping: An
701 Active Vision Cell for Three-Dimensional Plant Shoot Reconstruction. Plant Physiol.
702 2018;1–26.

703 38. Tippetts B, Lee DJ, Lillywhite K, Archibald J. Review of stereo vision algorithms and
704 their suitability for resource-limited systems. J Real-Time Image Process. 2016;11:5–25.

705 39. Xiong X, Yu L, Yang W, Liu M, Jiang N, Wu D, et al. A high-throughput stereo-imaging
706 system for quantifying rape leaf traits during the seedling stage. Plant Methods. 2017;13:1–
707 17.

708 40. Apelt F, Breuer D, Olas JJ, Annunziata MG, Flis A, Nikoloski Z, et al. Circadian, Carbon,
709 and Light Control of Expansion Growth and Leaf Movement. Plant Physiol. 2017;174:1949–
710 68.

711 41. Nguyen TT, Slaughter DC, Max N, Maloof JN, Sinha N. Structured light-based 3D
712 reconstruction system for plants. Sensors (Switzerland). 2015;15:18587–612.

713 42. Paulus S, Schumann H, Kuhlmann H, Léon J. High-precision laser scanning system for
714 capturing 3D plant architecture and analysing growth of cereal plants. Biosyst Eng.
715 2014;121:1–11.

716 43. Dornbusch T, Michaud O, Xenarios I, Fankhauser C. Differentially Phased Leaf Growth
717 and Movements in Arabidopsis Depend on Coordinated Circadian and Light Regulation.

718 Plant Cell. 2014;26:3911–21.

719 44. Dornbusch T, Lorrain S, Kuznetsov D, Fortier A, Liechti R, Xenarios I, et al. Measuring
720 the diurnal pattern of leaf hyponasty and growth in Arabidopsis a novel phenotyping
721 approach using laser scanning. *Funct Plant Biol.* 2012;39:860–9.

722 45. Paulus S, Eichert T, Goldbach HE, Kuhlmann H. Limits of active laser triangulation as an
723 instrument for high precision plant imaging. *Sensors (Switzerland).* 2014;14:2489–509.

724 46. Herrero-Huerta M, Lindenberg R, Gard W. Leaf Movements of Indoor Plants Monitored
725 by Terrestrial LiDAR. *Front Plant Sci.* 2018;9:189.

726 47. Thapa S, Zhu F, Walia H, Yu H, Ge Y. A novel LiDAR-Based instrument for high-
727 throughput, 3D measurement of morphological traits in maize and sorghum. *Sensors*
728 *(Switzerland).* 2018;18:1–14.

729 48. Woodham RJ. Photometric Method For Determining Surface Orientation From Multiple
730 Images. *Opt Eng.* 1980;19:139–44.

731 49. Smith LN, Zhang W, Hansen MF, Hales IJ, Smith ML. Innovative 3D and 2D machine
732 vision methods for analysis of plants and crops in the field. *Comput Ind.* 2018;97:122–31.

733 50. Zhang W, Hansen MF, Smith M, Smith L, Grieve B. Photometric stereo for three-
734 dimensional leaf venation extraction. *Comput Ind.* 2018;98:56–67.

735 51. Singh A, Ganapathysubramanian B, Singh AK, Sarkar S. Machine Learning for High-
736 Throughput Stress Phenotyping in Plants. *Trends Plant Sci.* 2016;21:110–24.

737 52. Pound MP, Atkinson JA, Townsend AJ, Wilson MH, Griffiths M, Jackson AS, et al.
738 Deep machine learning provides state-of-the-art performance in image-based plant
739 phenotyping. *Gigascience.* 2017;6:1–10.

740 53. Gonzalez N, Beemster GT, Inzé D. David and Goliath: what can the tiny weed
741 Arabidopsis teach us to improve biomass production in crops? *Curr Opin Plant Biol.*
742 2009;12:157–64.

743 54. De Vylder J, Vandenbussche F, Hu Y, Philips W, Van Der Straeten D. Rosette Tracker:
744 An Open Source Image Analysis Tool for Automatic Quantification of Genotype Effects.
745 Plant Physiol. 2012;160:1149–59.

746 55. Zhou J, Applegate C, Alonso AD, Reynolds D, Orford S, Mackiewicz M, et al. Leaf-GP:
747 An open and automated software application for measuring growth phenotypes for
748 arabidopsis and wheat. Plant Methods. 2017;13:1–17.

749 56. Tomé F, Jansseune K, Saey B, Grundy J, Vandenbroucke K, Hannah MA, et al. rosettr:
750 protocol and software for seedling area and growth analysis. Plant Methods. 2017;13:1–10.

751 57. Aich S, Stavness I. Leaf counting with deep convolutional and deconvolutional networks.
752 Proc - 2017 IEEE Int Conf Comput Vis Work ICCVW 2017. 2017;22–9.

753 58. Ren M, Zemel RS. End-to-End Instance Segmentation with Recurrent Attention. IEEE
754 Conf Comput Vis Pattern Recognit. 2016. p. 21–6.

755 59. Ubbens J, Cieslak M, Prusinkiewicz P, Stavness I. The use of plant models in deep
756 learning: An application to leaf counting in rosette plants. Plant Methods. 2018;14:1–10.

757 60. Yang H, Shao L, Zheng F, Wang L, Song Z. Recent advances and trends in visual
758 tracking: A review. Neurocomputing. 2011;74:3823–31.

759 61. Smeulders AWM, Chu DM, Cucchiara R, Calderara S, Dehghan A, Shah M. Visual
760 tracking: An experimental survey. IEEE Trans Pattern Anal Mach Intell. 2014;36:1442–68.

761 62. Azhar F, Emrith K, Pollard S, Smith M, Adams G, Simske S. Testing the Validity of
762 Lamberts Law for Micro-scale Photometric Stereo Applied to Paper Substrates. 2015;246–53.

763 63. Otsu N. A threshold selection method from gray-level histograms. IEEE Trans Syst Man
764 Cybern. 1979;9:62–6.

765 64. Jacquemoud S, Baret F. PROSPECT: A model of leaf optical properties spectra. Remote
766 Sens Environ. 1990;34:75–91.

767 65. Chelle M. Could plant leaves be treated as Lambertian surfaces in dense crop canopies to

768 estimate light absorption? *Ecol Modell.* 2006;198:219–28.

769 66. Karidas P, Challa KR, Nath U. The tarani mutation alters surface curvature in
770 *Arabidopsis* leaves by perturbing the patterns of surface expansion and cell division. *J Exp*
771 *Bot.* 2015;66:2107–22.

772 67. Sandalio LM, Rodríguez-Serrano M, Romero-Puertas MC. Leaf epinasty and auxin: A
773 biochemical and molecular overview. *Plant Sci.* 2016;253:187–93.

774 68. Edwards KD, Millar AJ. Analysis of circadian leaf movement rhythms in *Arabidopsis*
775 *thaliana*. *Methods Mol Biol.* 2007;362:103–13.

776 69. Mizoguchi T, Wheatley K, Hanzawa Y, Wright L, Mizoguchi M, Song H, et al. LHY and
777 CCA1 Are Partially Redundant Genes Required to Maintain Circadian Rhythms in
778 *Arabidopsis*. *Dev Cell.* 2002;2:629–41.

779 70. Doyle MR, Davis SJ, Bastow RM, McWatters HG, Kozma-Bognár L, Nagy F, et al. The
780 ELF4 gene controls circadian rhythms and flowering time in *Arabidopsis thaliana*. *Nature.*
781 2002;419:74–7.

782 71. Yoo SK, Hong SM, Lee JS, Ahn JH. A genetic screen for leaf movement mutants
783 identifies a potential role for AGAMOUS-LIKE 6 (AGL6) in circadian-clock control. *Mol*
784 *Cells.* 2011;31:281–7.

785 72. Jansen M, Gilmer F, Biskup B, Nagel KA, Rascher U, Fischbach A, et al. Simultaneous
786 phenotyping of leaf growth and chlorophyll fluorescence via GROWSCREENFLUORO
787 allows detection of stress tolerance in Simultaneous phenotyping of leaf growth and
788 chlorophyll fluorescence via GROWSCREEN FLUORO allows detection of stress tolera.
789 *Funct Plant Biol.* 2009;36:902–14.

790 73. De Vylder J, Vandenbussche F, Hu Y, Philips W, Van Der Straeten D. Rosette Tracker:
791 An Open Source Image Analysis Tool for Automatic Quantification of Genotype Effects.
792 *Plant Physiol.* 2012;160:1149–59.

793 74. Casal JJ. Shade Avoidance [Internet]. Arab. Book/American Soc. Plant Biol. 2012.

794 75. Pierik R, De Wit M. Shade avoidance: Phytochrome signalling and other aboveground
795 neighbour detection cues. *J Exp Bot.* 2014;65:2815–24.

796 76. Gommers CMM, Keuskamp DH, Buti S, van Veen H, Koevoets IT, Reinen E, et al.
797 Molecular Profiles of Contrasting Shade Response Strategies in Wild Plants: Differential
798 Control of Immunity and Shoot Elongation. *Plant Cell.* 2017;29:331–44.

799 77. Quint M, Delker C, Franklin KA, Wigge PA, Halliday KJ, Van Zanten M. Molecular and
800 genetic control of plant thermomorphogenesis. *Nat Plants.* 2016;2:1–9.

801 78. de Wit M, Ljung K, Fankhauser C. Contrasting growth responses in lamina and petiole
802 during neighbor detection depend on differential auxin responsiveness rather than different
803 auxin levels. *New Phytol.* 2015;208:198–209.

804 79. Vile D, Pervent M, Belluau M, Vasseur F, Bresson J, Muller B, et al. Arabidopsis growth
805 under prolonged high temperature and water deficit: Independent or interactive effects? *Plant,*
806 *Cell Environ.* 2012;35:702–18.

807 80. Crawford AJ, McLachlan DH, Hetherington AM, Franklin KA. High temperature
808 exposure increases plant cooling capacity. *Curr Biol.* 2012;22:R396–7.

809 81. Berry J, Bjorkman O. Photosynthetic Response and Adaptation to Temperature in Higher
810 Plants. *Annu Rev Plant Physiol.* 1980;31:491–543.

811 82. Bunce JA. Acclimation of photosynthesis to temperature in eight cool and warm climate
812 herbaceous C₃ species: Temperature dependence of parameters of a biochemical
813 photosynthesis model. *Photosynth Res.* 2000;63:59–67.

814 83. Yamori W, von Caemmerer S. Effect of Rubisco Activase Deficiency on the Temperature
815 Response of CO₂ Assimilation Rate and Rubisco Activation State: Insights from Transgenic
816 Tobacco with Reduced Amounts of Rubisco Activase. *Plant Physiol.* 2009;151:2073–82.

817 84. Wiese A, Christ MM, Virnich O, Schurr U, Walter A. Spatio-temporal leaf growth

818 patterns of *Arabidopsis thaliana* and evidence for sugar control of the diel leaf growth cycle.
819 New Phytol. 2007;174:752–61.

820 85. Smith AM, Stitt M. Coordination of carbon supply and plant growth. Plant, Cell Environ.
821 2007;30:1126–49.

822 86. Pyl E-T, Piques M, Ivakov A, Schulze W, Ishihara H, Stitt M, et al. Metabolism and
823 Growth in *Arabidopsis* Depend on the Daytime Temperature but Are Temperature-
824 Compensated against Cool Nights. Plant Cell. 2012;24:2443–69.

825 87. McClung CR. Plant Circadian Rhythms. Plant Cell Online. 2006;18:792–803.

826 88. Zielinski T, Moore AM, Troup E, Halliday KJ, Millar AJ. Strengths and limitations of
827 period estimation methods for circadian data. PLoS One. 2014;9:1–26.

828 89. He K, Gkioxari G, Dollar P, Girshick R. Mask R-CNN. 2017 IEEE Int Conf Comput Vis.
829 2017. p. 2980–8.

830 90. Lin TY, Maire M, Belongie S, Hays J, Perona P, Ramanan D, et al. Microsoft COCO:
831 Common objects in context. Lect Notes Comput Sci (including Subser Lect Notes Artif Intell
832 Lect Notes Bioinformatics). 2014;740–55.

833 91. Scharr H, Minervini M, French AP, Klukas C, Kramer DM, Liu X, et al. Leaf
834 segmentation in plant phenotyping: a collation study. Mach Vis Appl. 2016;27:585–606.

835 92. Henriques JF, Caseiro R, Martins P, Batista J. High-speed tracking with kernelized
836 correlation filters. IEEE Trans Pattern Anal Mach Intell. 2015;37:583–96.

837 93. Lucas BD, Kanade T. An Iterative Image Registration Technique with an Application to
838 Stereo Vision. Imaging Underst Work. 1981. p. 121–30.

839 94. Babenko B, Yang M-H, Belongie S. Visual Tracking with Online Multiple Instance
840 Learning. Comput Vis Pattern Recognit. 2009;983–90.

841 95. Allan D, Caswell T, Keim N, van der Wel C. trackpy: Trackpy v0.3.2 [Internet]. Zenodo.
842 2016. Available from: <http://doi.org/10.5281/zenodo.60550>

96. Bours R, Muthuraman M, Bouwmeester H, van der Krol A. OSCILLATOR: A system for analysis of diurnal leaf growth using infrared photography combined with wavelet transformation. *Plant Methods*. 2012;8:1–12.
97. van Zanten M, Voeselek LACJ, Peeters AJM, Millenaar FF. Hormone- and Light-Mediated Regulation of Heat-Induced Differential Petiole Growth in Arabidopsis. *Plant Physiol*. 2009;151:1446–58.
98. Kozuka T, Horiguchi G, Kim GT, Ohgishi M, Sakai T, Tsukaya H. The different growth responses of the Arabidopsis thaliana leaf blade and the petiole during shade avoidance are regulated by photoreceptors and sugar. *Plant Cell Physiol*. 2005;46:213–23.
99. Coppens F, Wuyts N, Inzé D, Dhondt S. Unlocking the potential of plant phenotyping data through integration and data-driven approaches. *Curr Opin Syst Biol*. 2017;4:58–63.
100. Araus JL, Kefauver SC, Zaman-Allah M, Olsen MS, Cairns JE. Translating High-Throughput Phenotyping into Genetic Gain. *Trends Plant Sci*. 2018;23:451–66.
101. Valmadre J, Bertinetto L, Henriques JF, Vedaldi A, Torr PHS. End-to-end representation learning for Correlation Filter based tracking. 2017 IEEE Conf Comput Vis Pattern Recognit. 2017. p. 5000–8.
102. Li L, Zhang Q, Huang D. A review of imaging techniques for plant phenotyping. *Sensors*. 2014;14:20078–111.

FIGURE LEGENDS

Figure 1. Capturing dynamic plant growth traits using photometric stereo imaging. (A) PS comprises a circular arrangement of NIR LEDs with a central camera positioned above the plant(s). Red-dashed lines show the direction of light vectors. (B, C) Assembled PS-Plant system shown from side and top views. Each LED is attached to a dedicated heatsink and

angled at 30° using a custom 3D printed bracket to minimise the light distribution across the field of view. Both the camera and light sources are stationary.

Figure 2. Evaluating the accuracy of PS-Plant with 2D and 3D data. (A, B) The estimated area and inclination angle of a flat, matte object (600 mm²) from 0° to 45° at 5° intervals. Each data point represents the average of thirty randomly selected regional patches of varying size (35-600 mm²). (C, D) The area of three similarly sized Arabidopsis whole rosettes (750 ± 13.5 mm²) and leaf inclination angles were estimated from 0-45° at 5° intervals. The dashed-black lines indicate ground truth measurements. Error bars represent ±SD of the means.

Figure 3. Data outputs of PS-Plant for Arabidopsis. (A) Surface normal map (top) rendered for a wild-type Arabidopsis rosette used to derive models for surface inclination (middle) and convexity (bottom). (B) Projected rosette area estimates captured for wild-type plants under standard growth conditions (22 °C, 150 µmol photons m⁻² s⁻¹, 12 : 12 h light : dark) for 2D and 3D data from the mean ± SE values of 13 biological replicates. (C) Percentage difference between 2D and 3D estimations. (D) Estimated rosette mean inclination angles across the rosette surface. (E-H) Circularity, compactness, diameter and perimeter estimates derived from 2D data.

Figure 4. PS-Plant shows that Arabidopsis plants grown under different conditions show differences in growth architecture. (A) Wild-type Arabidopsis plants (24 DAG) following growth under nine different light and temperature conditions. (B) Estimated 3D projected rosette area growth of rosettes grown under the different environments. (C-E) Estimated 3D projected area, fresh weights and leaf count for rosettes at 24 DAG. (F-H) The average relative expansion rate (RER) during light and dark periods for each growth condition (calculated from

15-18 DAG with a 4 hr sliding window). Values represent the mean \pm SE values of at least three biological replicates. Asterisks indicate significant differences between light and dark values for each condition based on Student's t-test ($p < 0.05$). The colour legends in **A** are applicable to **B**, and **F-H**.

Figure 5. Arabidopsis plants grown under different conditions show differences in circadian movement. (**A-C**) The relative rosette surface inclination (i.e. rosette surface inclination following baseline detrending and alignment to the mean) for plants grown in high, medium and low light from 15-18 DAG (see Supplementary Figure S3 for full data sets). (**D**) Period, phase and amplitude calculated by the MFourFit method [88] using data from 11-24 DAG. Values are the mean \pm SD of measurements made on at least three biological replicates. Values within each column followed by different letters are significantly different from each other and values followed by the same letter are not ($P < 0.05$) as determined by ANOVA followed by Tukey's HSD tests.

Figure 6. Automated segmentation of individual Arabidopsis leaves using PS-Plant data. Examples are shown based on the Mask R-CNN architecture for plants grown in ML at three different temperatures. (**A**) Composite input images are composed of surface normals in x, y directions and albedo data. (**B**) Manually labelled images (ground truth) used for training. (**C**) Mask R-CNN outputs images showing automated leaf segmentation. For ground truth images and Mask-RCNN outputs each leaf was assigned a unique arbitrary colour.

Figure 7. Automated tracking of leaf labels from segmented Arabidopsis rosettes. (**A**) Three consecutive frames for labelled leaves produced using the trained Mask R-CNN architecture (as in Fig. 6). (**B**) Tracked leaves retained the same colour after applying label

tracking (see Rich Media 4). The particle filter allowed calibration of a variety of parameters, including span (the velocity of 'span + 1' recent frames), search radius (the furthest distance (in pixels) an object may travel between frames), frame memory (the maximum number of frames a seen/tracked object that is absent will be remembered) and filter (the minimum number of frames an object must be seen/tracked to be included). The following particle filter settings produced the best results: span (10), search radius (30), frame memory (3) and filter (100). (C) Example of leaf tracking using leaf centroid locations. Each coloured line represents the movement of the centroid location of an individual leaf from 11 to 24 DAG.

Figure 8. Analyses of growth and movement for individual leaves. (A) Key landmarks for leaf analysis: rosette origin (P_o), leaf base/leaf blade and petiole intersection point (P_B) and leaf tip (P_T). Data are shown from plants grown in ML at three different temperatures [17 °C (LT) 22 °C (MT) or 27 °C (HT)]. (B, C) Leaf blade area and mean surface inclination of a maturing leaf (leaf 1) and an immature leaf (leaf 4) from 15 to 18 DAG. Error bars represent the mean \pm SE of three separate leaves. (D) Period, phase and amplitude values of the leaf blade from immature leaves (leaves 3 and 4; $n = 6$ leaves). Letters above the error bars indicate significant differences within each data type ($p < 0.05$) as determined by ANOVA followed by Tukey's HSD tests. Data sets with the same letter are not significantly different. (E) The ratio of leaf blade: petiole length for leaves 1 to 4 (L1 to L4). Values represent the mean ratio over 24 hr (17-18 DAG) for three separate leaves. Letters indicate significant differences ($p < 0.05$) within each leaf data set for different temperatures (i.e. L1, L2, L3 and L4).

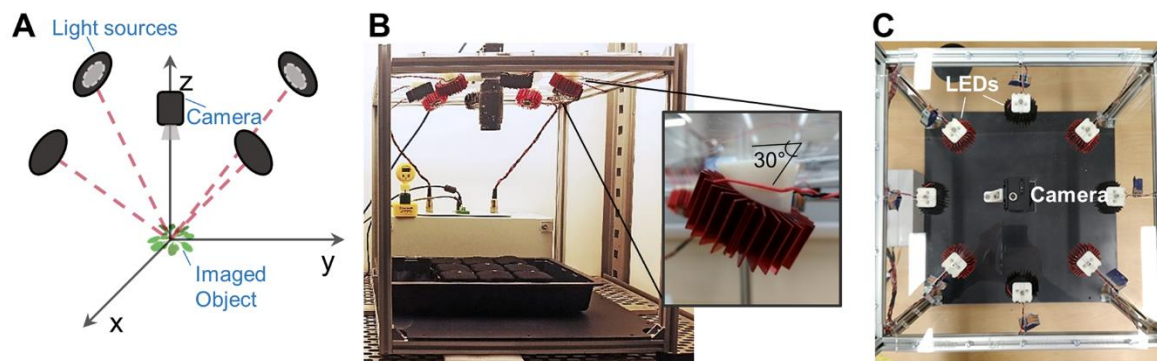


Figure 1.

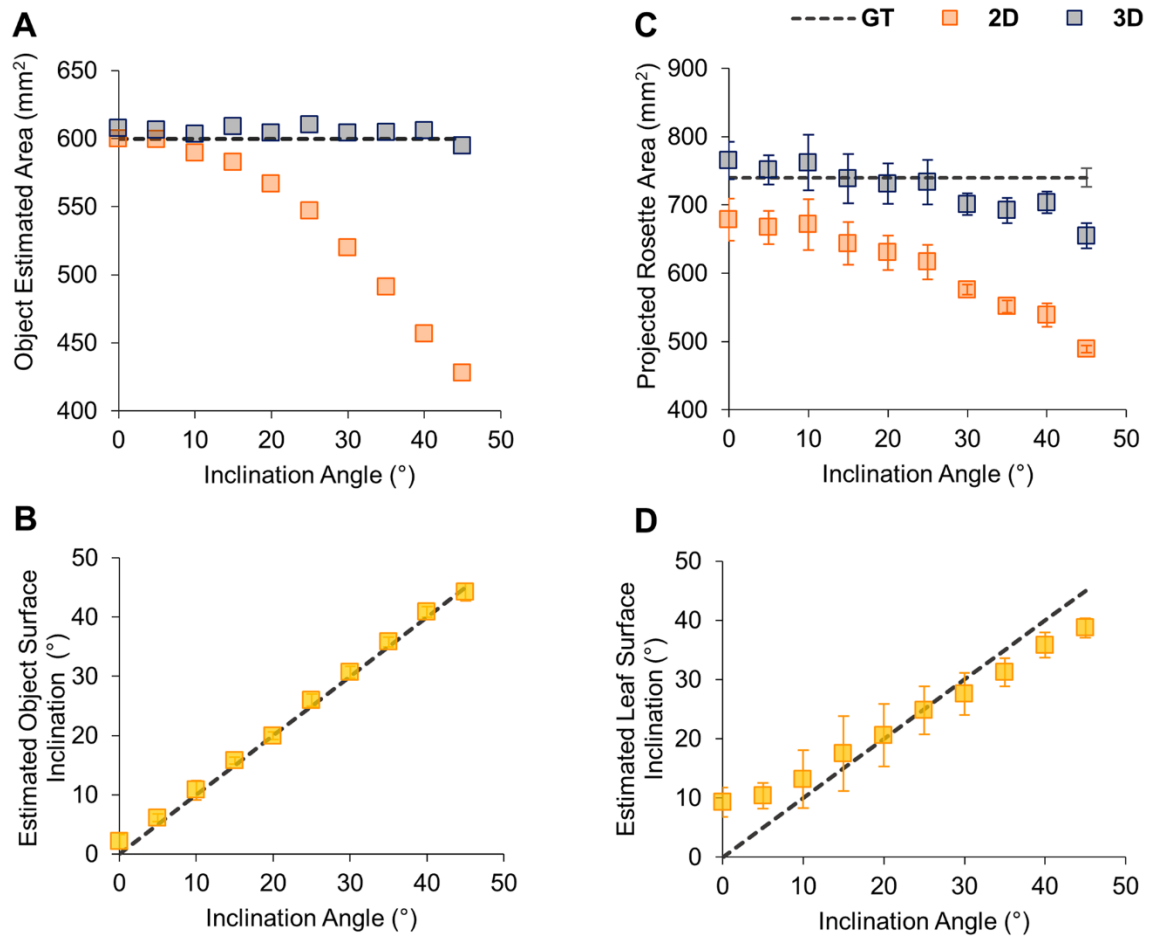


Figure 2.

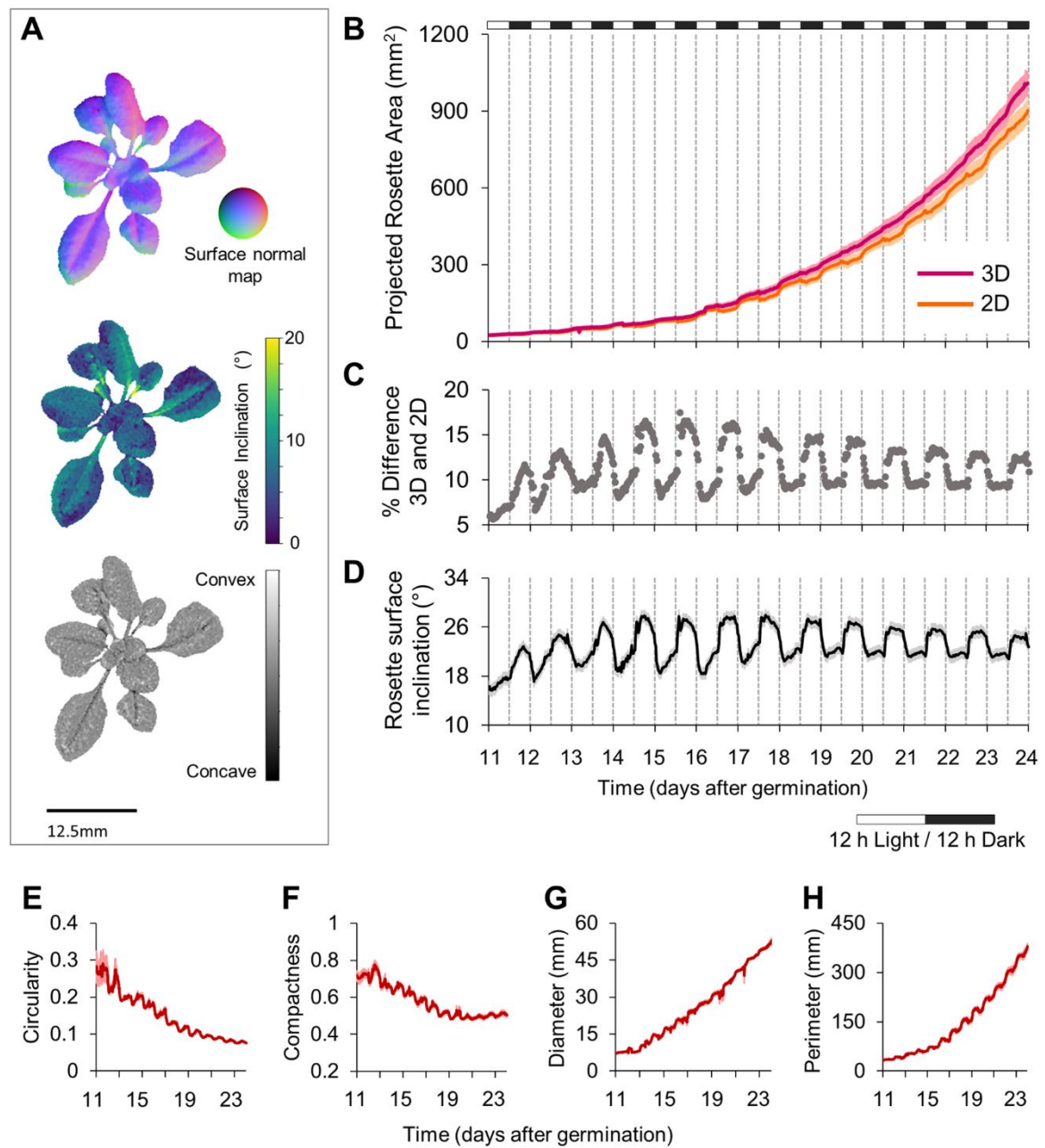


Figure 3.

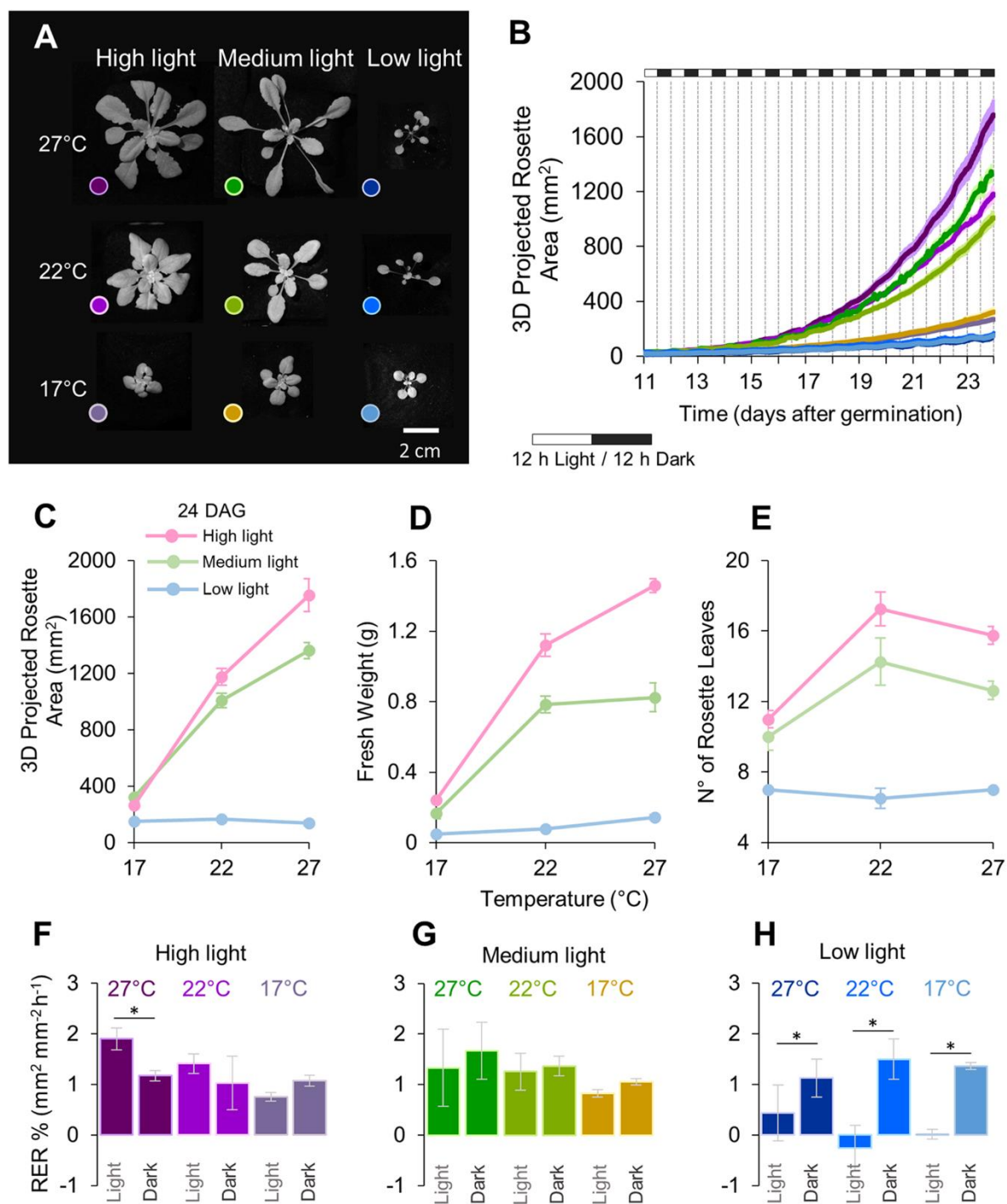
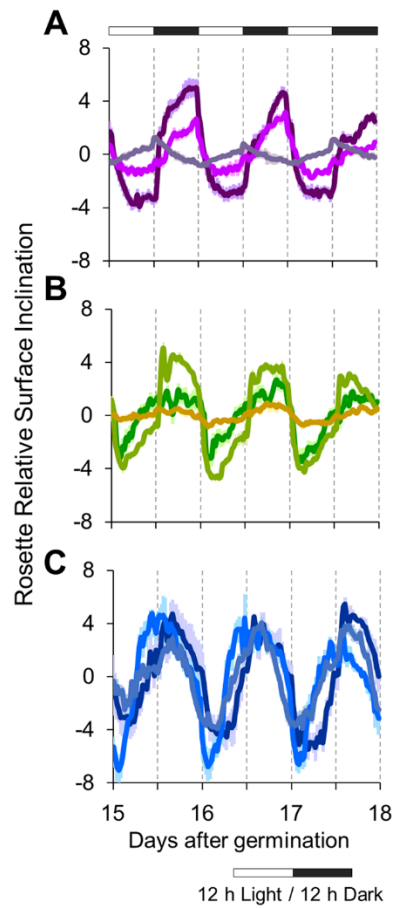


Figure 4.



D

Treatment	Period (h)	Phase (h)	Amplitude (°)	
High Light	27 °C	24.1 ± 0.2 ^a	21.9 ± 1.0 ^{ab}	2.7 ± 0.2 ^b
	22 °C	24.0 ± 0.1 ^a	23.1 ± 0.8 ^a	1.6 ± 0.5 ^c
	17 °C	24.5 ± 0.4 ^a	10.5 ± 2.4 ^f	1.0 ± 0.4 ^{cd}
Medium Light	27 °C	24.1 ± 0.1 ^a	17.9 ± 2.0 ^{cd}	2.6 ± 0.3 ^b
	22 °C	24.1 ± 0.1 ^a	18.9 ± 1.2 ^{bc}	3.2 ± 0.6 ^{ab}
	17 °C	24.3 ± 0.4 ^a	15.1 ± 3.6 ^{de}	0.5 ± 0.1 ^d
Low Light	27 °C	24.1 ± 0.1 ^a	15.4 ± 1.3 ^{cde}	3.4 ± 0.7 ^{ab}
	22 °C	24.3 ± 0.2 ^a	11.9 ± 2.2 ^{ef}	3.7 ± 0.3 ^a
	17 °C	24.1 ± 0.1 ^a	15.0 ± 0.8 ^{de}	2.8 ± 0.6 ^{ab}

Figure 5.

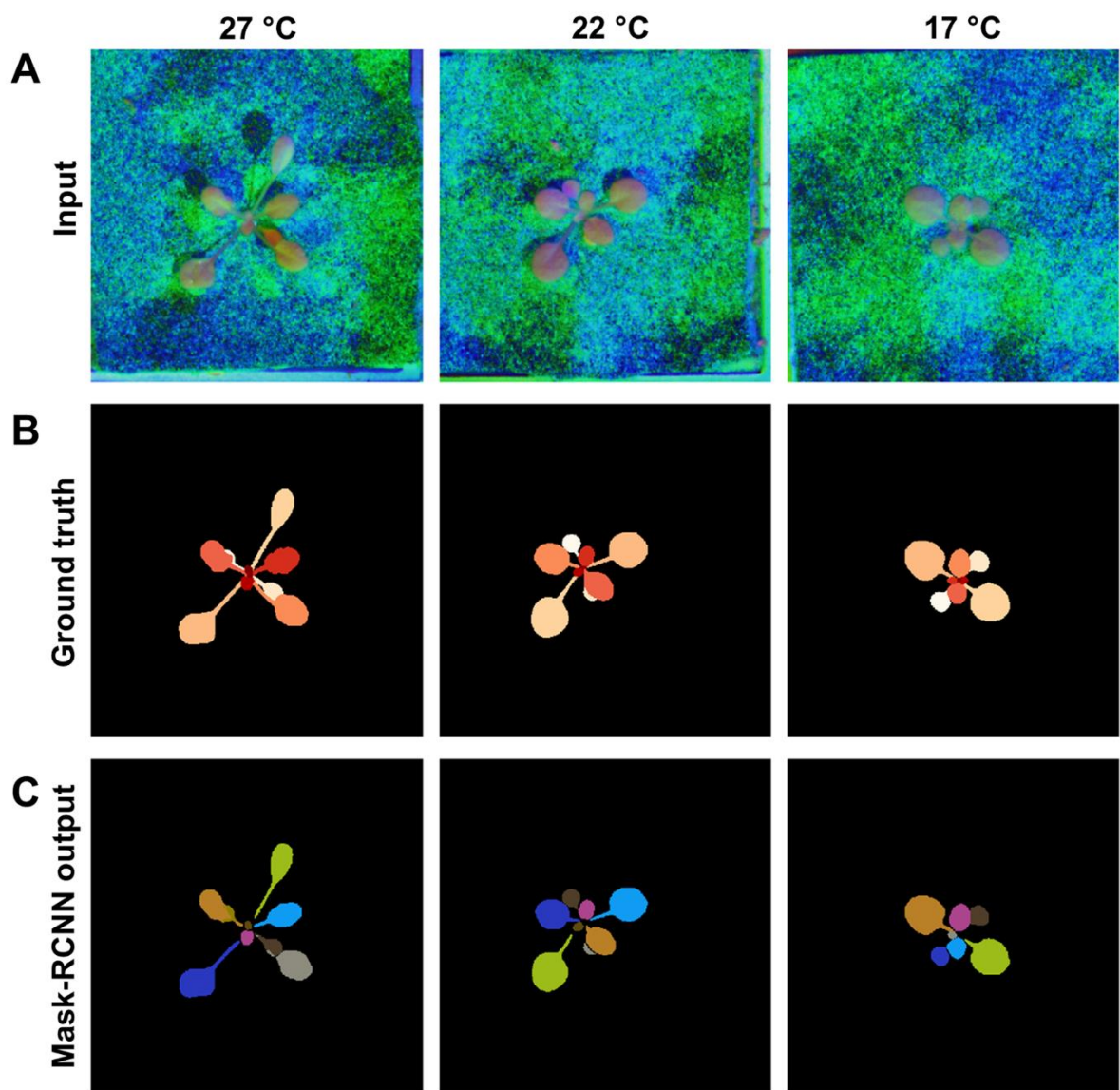


Figure 6.

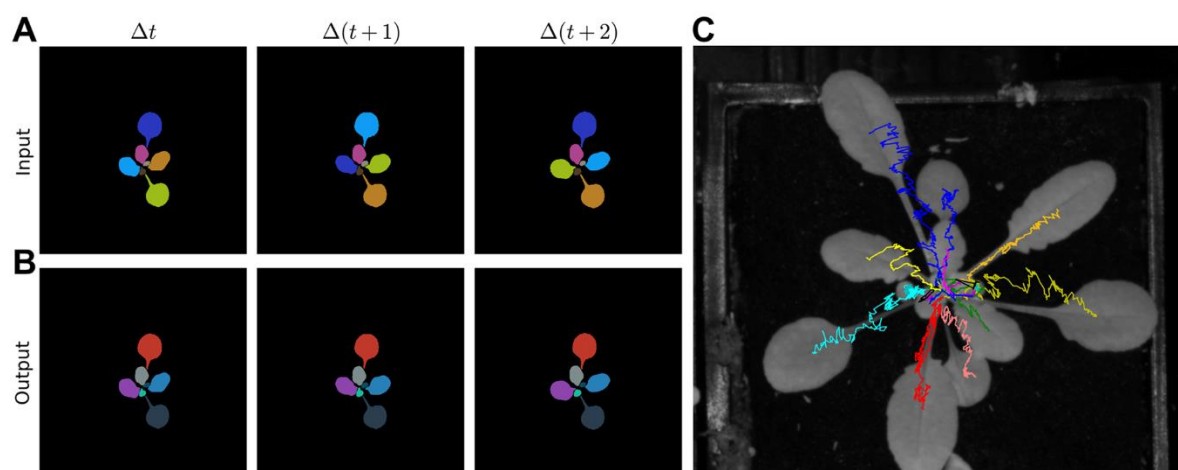


Figure 7.

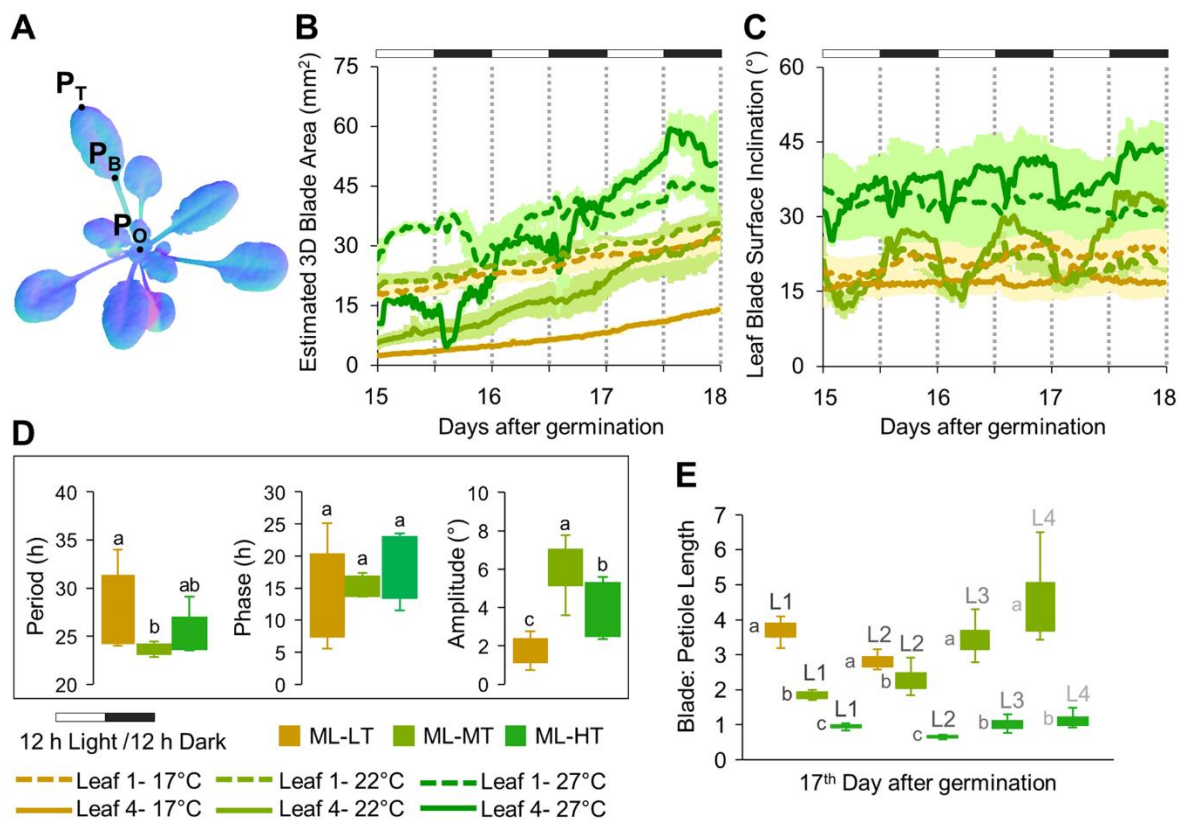


Figure 8.